



Highly flexible and transparent film heaters based on colorless polyimide substrate with a GZO/AgNW/GZO sandwich structure

Runfei Wang^{1,2} · Peizhi Cai³ · Wei Xu² · Ruiqin Tan³ · Wenfeng Shen² · Zhaozhao Wang² · Guofei Chen² · Jian Huang¹ · Xingzhong Fang² · Weijie Song^{2,4}

Received: 7 October 2019 / Accepted: 31 January 2020 / Published online: 10 February 2020
© Springer Science+Business Media, LLC, part of Springer Nature 2020

Abstract

In the past years, transparent film heaters (TFHs) based on silver nanowires (AgNWs) have attracted much attention because of their high transmittance, excellent flexibility, and great thermal response. In this paper, we fabricated flexible TFHs with a sandwich structure composed of Ga-doped ZnO (GZO) and AgNWs on the colorless polyimide (cPI) substrate. The optimized hybrid film exhibited a sheet resistance of $14.6 \Omega \text{ sq}^{-1}$ with a transmittance of 79%. Excellent thermal uniformity and heating stability of TFHs were demonstrated. The thermal response tests of the GZO/AgNW/GZO/cPI TFHs showed high saturation temperature ($\sim 176 \text{ }^\circ\text{C}$) with low input voltage ($\sim 6 \text{ V}$), fast response time ($\sim 15 \text{ s}$), and stable heating performance. These results indicate that the flexible TFHs with a GZO/AgNW/GZO sandwich structure have broad potential applications in flexible electronic devices.

1 Introduction

Transparent film heaters (TFHs) have received much attention in recent years, due to their wide applications in wearable devices [1–3], defogging windows [4, 5], and thermochromic display [6]. The commonly used transparent conductive material (TCM) in TFHs was indium tin oxide (ITO), because of its high transparency and high

conductivity [7]. However, brittleness and indium scarcity restricted the application of ITO in flexible TFHs. Furthermore, ITO exhibited a low-temperature response because of its intrinsic nature [8]. To overcome these problems, various alternative TCMs, such as other metal oxides [9], metal nanowires [10], graphene [11], and carbon nanotubes [12, 13], have been widely studied. Among them, TFHs based on silver nanowires (AgNWs) percolation network have advantages of high transmittance, excellent electrical conductivity, outstanding flexibility, and highly thermal response, as well as easily fabricated by low-cost and large-scale non-vacuum processes [14].

However, AgNW-based TFHs suffer several inherent drawbacks, including poor thermal uniformity [15], instability at a relatively high applied voltage [16], and harsh environments [17]. Covering AgNW percolation network with a metal-oxide layer to form a hybrid structure has been suggested as a promising alternative to overcome these problems. Cheong et al. reported an ITO/AgNW heater with $T = 85.1\%$ and $R_s = 50.9 \Omega \text{ sq}^{-1}$. Comparing to the bare AgNWs, the hybrid TFHs showed higher temperature and more uniform heating [18]. Our previous work revealed that the hybrid TCM on PET substrate have great optoelectrical properties and mechanical stability [19]. Moreover, colorless polyimide (cPI) with high transparency and high glass transition temperature (T_g) was used instead of PET and improved the thermostability of TFHs [20].

Electronic supplementary material The online version of this article (<https://doi.org/10.1007/s10854-020-03031-4>) contains supplementary material, which is available to authorized users.

- ✉ Wei Xu
weix@nimte.ac.cn
- ✉ Ruiqin Tan
tanruiqin@nbu.edu.cn
- ✉ Weijie Song
weijiesong@nimte.ac.cn

- ¹ School of Material Science and Engineering, Shanghai University, Shanghai 200444, China
- ² Ningbo Institute of Materials Technology and Engineering, Chinese Academy of Sciences, Ningbo 315201, China
- ³ Faculty of Electrical Engineering and Computer Science, Ningbo University, Ningbo 315211, China
- ⁴ Center of Materials Science and Optoelectronics Engineering, University of Chinese Academy of Sciences, Beijing 100049, China

Ga-doped zinc oxide (GZO) was a promising alternative to ITO, because of its good optoelectronic performance, low effective cost, and non-toxicity [21]. In this work, we successfully fabricated flexible TFHs with a sandwich structure of GZO/AgNW/GZO/cPI. The GZO layers were prepared at room temperature by radio frequency (RF) magnetron sputtering and AgNWs were deposited through rod-coating procedure. The hybrid films performed good stability in harsh environment with the protection of GZO layer to reduce the contact of the AgNWs with air during heating. The fabricated flexible TFHs exhibited great heating performance and highly uniform heat distribution over the areas.

2 Experimental procedures

2.1 Materials

Poly(vinylpyrrolidone) (PVP) (MW = 58,000), PVP (MW = 360,000), ethylene glycol (EG), silver nitrate (AgNO_3), and ferric chloride (FeCl_3) were all purchased from Shanghai Aladdin industrial Co., Ltd. All chemicals were of analytical grade and used as received without further purification.

2.2 Synthesis of AgNWs

AgNWs were synthesized through a modified polyol method [22]. Approximately 0.4 g of both PVP was added to 120 mL of EG in the flask at room temperature, followed by 1.0 g of AgNO_3 . After complete dissolution, 300 μL of FeCl_3 solution (154 μM in EG) was added to the mixture and stirred for 20 min. The solution was then immediately heated to 130 $^\circ\text{C}$ and stirred vigorously for 10 min. The reaction continued for another 2 h without stirring. Then, the reaction product was washed by centrifugation with acetone and ethanol to remove the solvent, PVP, and other impurities. Finally, AgNWs were dispersed in ethanol for future use.

2.3 Fabrication of GZO/AgNW/GZO/cPI hybrid film

A schematic of the fabrication process is shown in Fig. 1. The GZO/AgNW/GZO sandwich structure was prepared on the surface of cPI substrate. Both bottom and top GZO layers were sputtered using a home-made GZO target with a contrast RF power of 200 W, an Ar flow of 30 sccm, and a working pressure of 3 mTorr. The bottom GZO layer was used to improve the wettability between AgNW suspension and cPI substrate to obtain uniform AgNW networks. The AgNW interlayer was deposited on the bottom GZO layer by rod-coating. The density of AgNW interlayer was controlled by the cycles (N) of rod-coating.

2.4 Characterization and measurement

The surface morphologies of GZO/AgNW/GZO/cPI hybrid films were examined using a scanning electron microscopy (SEM, Hitachi, S-4800). The optical transmittances of the as-prepared hybrid films were observed by a UV–Vis spectrophotometer (PerkinElmer, Lambda 950) with an integrating sphere. The sheet resistance was measured by a four-point probe system (Napson Corp., Cresbox). The mechanical stability test was performed using a lab-made bending test machine. The heaters were supplied by a DC power source (LODESTAR, DC POWER SUPPLY LPS305D) and the real-time temperature during working was monitored using an infrared thermometer (SMART SENSOR, AR842A). The heat distribution of TFHs was captured by an infrared camera (FLIR, E85).

3 Results and discussion

3.1 Morphologies of GZO/AgNW/GZO/cPI hybrid films

Figure 2 shows the SEM images of GZO/AgNW/GZO/cPI hybrid films with different rod-coating cycles (N) of AgNWs. As shown in Fig. 2a, a highly uniform and dense

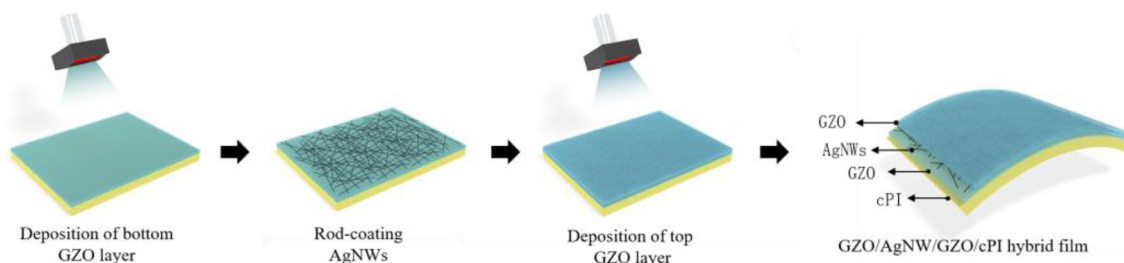


Fig. 1 Schematic of the fabrication of GZO/AgNW/GZO/cPI hybrid film

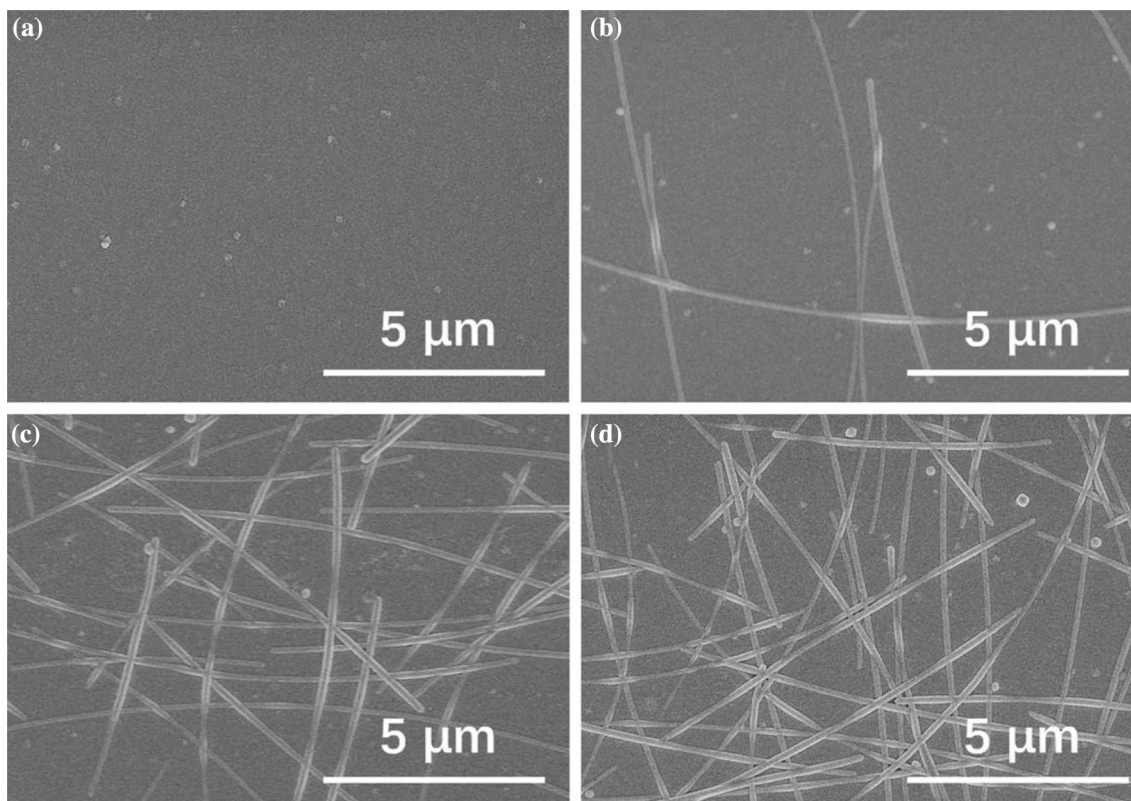


Fig. 2 SEM images of the GZO/AgNW/GZO/cPI hybrid films with different rod-coating cycles (N) of AgNWs. **a** $N=0$, **b** $N=1$, **c** $N=3$, **d** $N=5$

GZO layer was formed on the cPI substrate. As shown in Fig. 2b–d, the density of AgNWs increased as N increased from 1 to 5. Randomly percolated and well-connected network of AgNWs is also demonstrated in Fig. 2b–d. The average length and diameter of AgNWs were 100 nm and 20 μm , respectively.

3.2 Optical and electrical properties of GZO/AgNW/GZO/cPI hybrid films

Figure 3a shows the optical transmittance spectra (including cPI substrate) of the hybrid films with different N . The corresponding sheet resistance (R_s) of each film is listed in Table 1. The pure GZO film with R_s of $173.6 \Omega \text{ sq}^{-1}$ obtained a high optical transmittance at 550 nm (T_{550}) of 88%. The optical transmittance of hybrid films decreased as the number of N increased. As shown in Fig. 3a, the T_{550} of GZO/1 AgNW/GZO ($N=1$) exhibited 85%. As N increased to 5, the T of the hybrid film decreased to 79%. This is mainly due to the light reflection and scattering from both the AgNW interlayer and the AgNW/GZO interface. With the optical transmittance of hybrid films decreased as the number of N increased, the color of the hybrid films gradually turned yellow, as shown in Fig. 3b. The R_s of the hybrid films decreased as N increased, as shown in Fig. 3c. The

sample with $N=1$ displayed a R_s of $79.1 \Omega \text{ sq}^{-1}$, whereas the sample with N of 5 decreased to $14.6 \Omega \text{ sq}^{-1}$. These results indicated that the optical and electrical properties of GZO/AgNW/GZO/cPI hybrid films can be tuned by the density of AgNW percolation networks.

As published in previous work, the electrical contribution of the AgNW film in R_s of GZO/AgNW/GZO/cPI hybrid film was elucidated by the following equation [23]:

$$\frac{1}{R_s} = \frac{2}{R_{\text{GZO}}} + \frac{1}{R_{\text{AgNW}}}, \quad (1)$$

where R_{GZO} and R_{AgNW} are the sheet resistances of GZO film and AgNW film, respectively. In this work, R_{GZO} was nearly constant. R_{AgNW} was justified by changing rod-coating cycles N . As deduced from Eq. (1), when R_{AgNW} decreased with increasing N , R_s of the hybrid film decreased as well. The phenomenon revealed in our results agreed with the predictions of Eq. (1).

The figure of merit (Φ) was used to estimate the electro-optical performance of the hybrid films, which was calculated from the Haacke equation [24].

$$\phi = \frac{T_{550}^{10}}{R_s}. \quad (2)$$

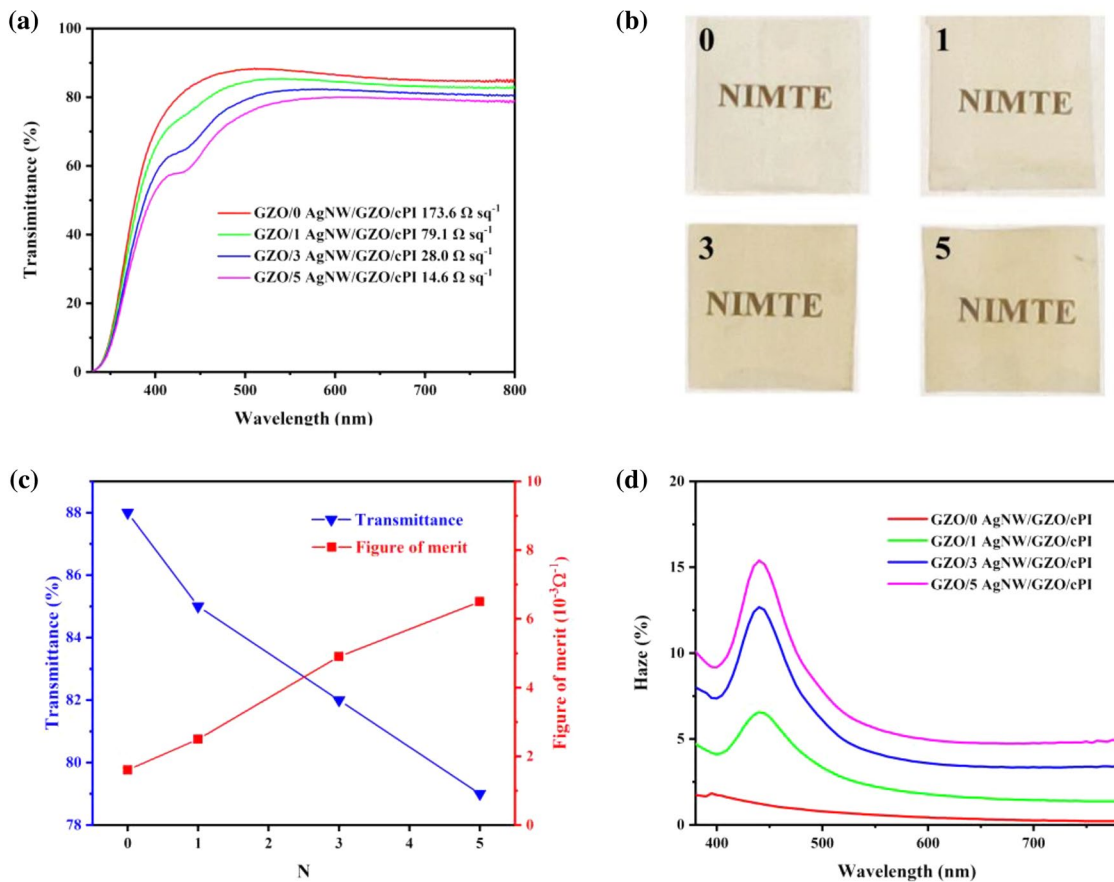


Fig. 3 **a** Optical transmittance, sheet resistance, and **b** photographs of transparent GZO/AgNW/GZO/cPI hybrid films. **c** Relationship between N , transmittance at 550 nm, and figure of merit. **d** The haze

curves of GZO/cPI film and GZO/AgNW/GZO/cPI hybrid films with different rod-coating cycles

Table 1 Comparison of the electrical and optical properties of the GZO/cPI film and GZO/AgNW/GZO/cPI hybrid films

N	T_{550} (%)	R_s (Ω sq ⁻¹)	H_a (%)	Φ (10^{-3} Ω^{-1})
0	88	173.6	0.66	1.6
1	85	79.1	2.74	2.5
3	82	28.0	5.36	4.9
5	79	14.6	13.83	6.5

As shown in Fig. 3c, the optimal GZO/AgNW/GZO/cPI hybrid film with N of 5 possessed a Φ value of $6.5 \times 10^{-3} \Omega^{-1}$, which was larger than our previously reported value of AZO/AgNW/AZO on a PET or PI substrate [19, 25].

Haze is another important factor to quantify the optical parameters of transparent conduct films. Figure 3d shows the haze property of the as-prepared hybrid films. The average haze values of hybrid films from 380 to 780 nm (H_a) are listed in Table 1. The pure GZO film exhibits relatively low haze due to the smooth surface and its low

light scattering. With adding of AgNWs, the haze values of hybrid films increased before wavelength of 450 nm, and then gradually decreased across the visible spectrum. This is mainly because AgNWs interacted with short wavelength part of the visible light. It is deduced that the haze of hybrid films can also be finely tuned by varying AgNW density. For instance, the H_a of GZO/5 AgNW/GZO reached 13.83%, which is five times that of GZO/1 AgNW/GZO (2.74%).

3.3 Mechanical properties of GZO/AgNW/GZO/cPI hybrid films

Mechanical properties of pure GZO/cPI film and GZO/AgNW/GZO/cPI hybrid films were tested by a lab-made bending test machine, as shown in the inset of Fig. 4a. The bending radius was about 2 mm, as shown in Fig. 4b, and the bending frequency was 1.5 Hz. The rate of resistance change (R_c) can be expressed as Eq. (3), where R_0 is the initial resistance and R is the resistance after bending.

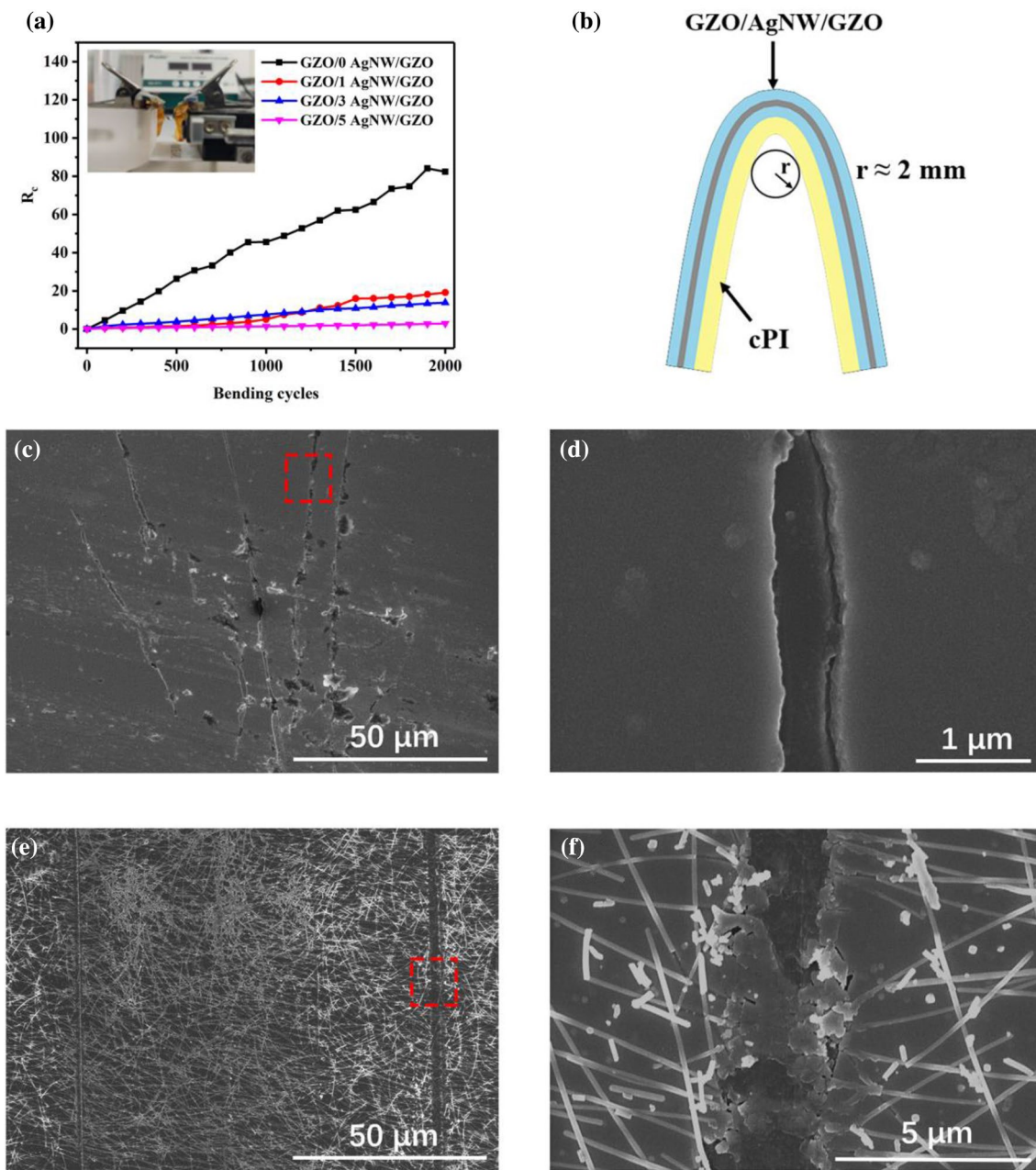


Fig. 4 **a** Resistance change in the pure GZO/cPI and GZO/AgNW/GZO/cPI hybrid films. Inset is the photograph of lab-made test machine. **b** The schematic diagram of the calculation of the bending

radius. SEM images of **c, d** GZO/cPI film and **e, f** GZO/5 AgNW/GZO/cPI hybrid film after 2000 cycles of the bending test

$$R_c = \frac{R - R_0}{R_0} \tag{3}$$

R_c as a function of bending cycles for the pure GZO and GZO/AgNW/GZO/cPI hybrid films is shown in Fig. 4a. After 2000 bending cycles, the resistance of the GZO/cPI film increased dramatically, and the R_c value was 82.3. In

contrast, the value of R_c for the GZO/5 AgNW/GZO/cPI hybrid film after 2000 bending cycles was only 2.9.

The considerable reduction in the value of R_c for the hybrid film was attributed to the flexibility imparted by the AgNW percolation network embedded between GZO films, which was confirmed by analyzing the surface morphologies of the hybrid film after bending test. As shown in Fig. 4c, the

pure GZO film cracked after 2000 cycles of the outer bending test, which resulted in a sharply increasing in R_c of the film. There were more cracks in the pure GZO film and the spacing distances were closer than those of the hybrid film. As shown in the magnified view of Fig. 4d, there was no contact between pure GZO cracks. In comparison, the hybrid film still maintained an integral conductive network after bending test and few cracks could be found on the surface, as shown in Fig. 4e and f. This phenomenon is attributed to the flexible and ductile nature of the AgNWs, which in turn enhance the flexibility of the hybrid films.

3.4 Electrothermal properties of GZO/AgNW/GZO/cPI hybrid films

To understand the nature of Joule heating in the TFHs, the temperature properties of GZO/AgNW/GZO/cPI hybrid films with size of 2.0 cm × 2.0 cm were analyzed. Figure 5a presents the thermal response behavior of GZO/AgNW/GZO/cPI hybrid TFHs with different numbers of rod-coating cycles at a constant bias of 4 V. A higher steady-state temperature (T_s) of TFHs is obtained with the growing N at a given input voltage. The maximum T_s for the TFH of GZO/5 AgNW/GZO/cPI reached 106.4 °C, while that of GZO/1 AgNW/GZO/cPI reduced to 48.9 °C. Figure 5b shows the time-dependent temperature of GZO/AgNW/GZO/cPI TFHs with different N for stepwise increased voltage. The input voltage increased from 1 to 6 V with the step of 1 V in every 85 s and the temperature increased with the incremental applied potential. The increment of T_s for TFH with higher resistance was lower than that with lower resistance.

Figure 5c shows the time-dependent temperature profiles of the GZO/5 AgNW/GZO/cPI hybrid film, which is plotted with respect to the stepwise increased input voltage from 1 to 6 V with steps of 1 V. The T_s of the TFH reached 29.0 °C when the input voltage was set at 1 V. When the applied voltage increased to 6 V, the T_s reached above 170.0 °C, confirming its good performance at a low input voltage. Higher T_s at a low input voltage implied an efficient conversion of electrical energy into Joule heating. The uniform temperature distribution on the TFH of GZO/5 AgNW/GZO/cPI was obtained from the IR photograph, as shown in the inset of Fig. 5c.

The response time, which is defined as the time required to reach T_s from room temperature, is one of the key factors for evaluating the performance of TFHs. As shown in Fig. 5d, the T_s of GZO/5 AgNW/GZO/cPI TFH reached 99.7 °C in less than 15 s at 4 V applied voltage, demonstrating the fast response of the device. The heating and cooling rate of the GZO/5 AgNW/GZO/cPI TFH as a function of time is shown in the inset of Fig. 5d. The maximal heating and cooling rate of GZO/5 AgNW/GZO/cPI TFH was calculated to be 17.6 °C s⁻¹ and 15.7 °C s⁻¹, respectively.

Comparison of thermal properties between our TFH and other TFHs reported before is listed in Table S1 in Supplementary Information.

In order to understand the concrete mechanism, the curve of $1/\Delta T - 1/U^2$ is plotted in Fig. 5e. According to Eq. (4), the steady-state temperature of the TFH is decided by the input voltage [26], which was demonstrated by our experimental data.

$$\frac{1}{\Delta T} = \alpha + \frac{hAR_0}{U^2}, \quad (4)$$

where ΔT is the difference between steady-state temperature (T_s) and initial temperature (T_0), α is the temperature coefficient of resistance, h is the total heat transfer coefficient which includes the AgNW networks and substrate, A is the surface area, R_0 is the initial resistance, and U is the input voltage.

Another important parameter to evaluate the heating performance of the TFH is power consumption, which can be described as Eq. (5) [27]:

$$T_s = T_0 + \frac{2P}{hA + \sqrt{4\alpha^2 P^2 + h^2 A^2}}. \quad (5)$$

As shown in Fig. 5f, the experiment data of steady-state temperature and input power (P) were fitted well according to Eq. (5), which revealed a non-linear relationship.

On/off cycle response of the TFH with the numbers of rod-coating cycles ($N=5$) under the input voltage of 4 V was conducted. As shown in Fig. 6a, stability tests under electrical stress at 4 V bias for 100 cycles showed no significant degradation of achievable temperature, both of which manifested the stability for repeated and long-term use. The slight increase of the maximum temperature, as shown in Fig. 6b, indicated a slight decrease of heater resistance. This phenomenon could be ascribed to more closely connected nanowires during the heating process.

In order to investigate the stability of the hybrid film with the protection of GZO layer in harsh environment, the AgNW/GZO (without deposition of top GZO layer) and the GZO/AgNW/GZO hybrid films were evaluated by an accelerated test by keeping films under an oven at 85 °C and a relative humidity (RH) of 85% for 24 h. As shown in Fig. 7a, the resistances of the AgNW/GZO and the GZO/AgNW/GZO hybrid films increased consistently over 24 h ascribed to the surface oxidation. GZO/AgNW/GZO hybrid film shows a lower resistance change than AgNW/GZO. The variations in resistance for AgNW/GZO and GZO/AgNW/GZO TFHs were 83% and 48%, respectively. Since the GZO layer is not completely dense, oxygen and water can contact the AgNWs in harsh environment, resulting in an increase in the resistance. The GZO layer still has a good protection compared to the hybrid film without sputtering the top layer of GZO, as illustrated in Fig. 7b.

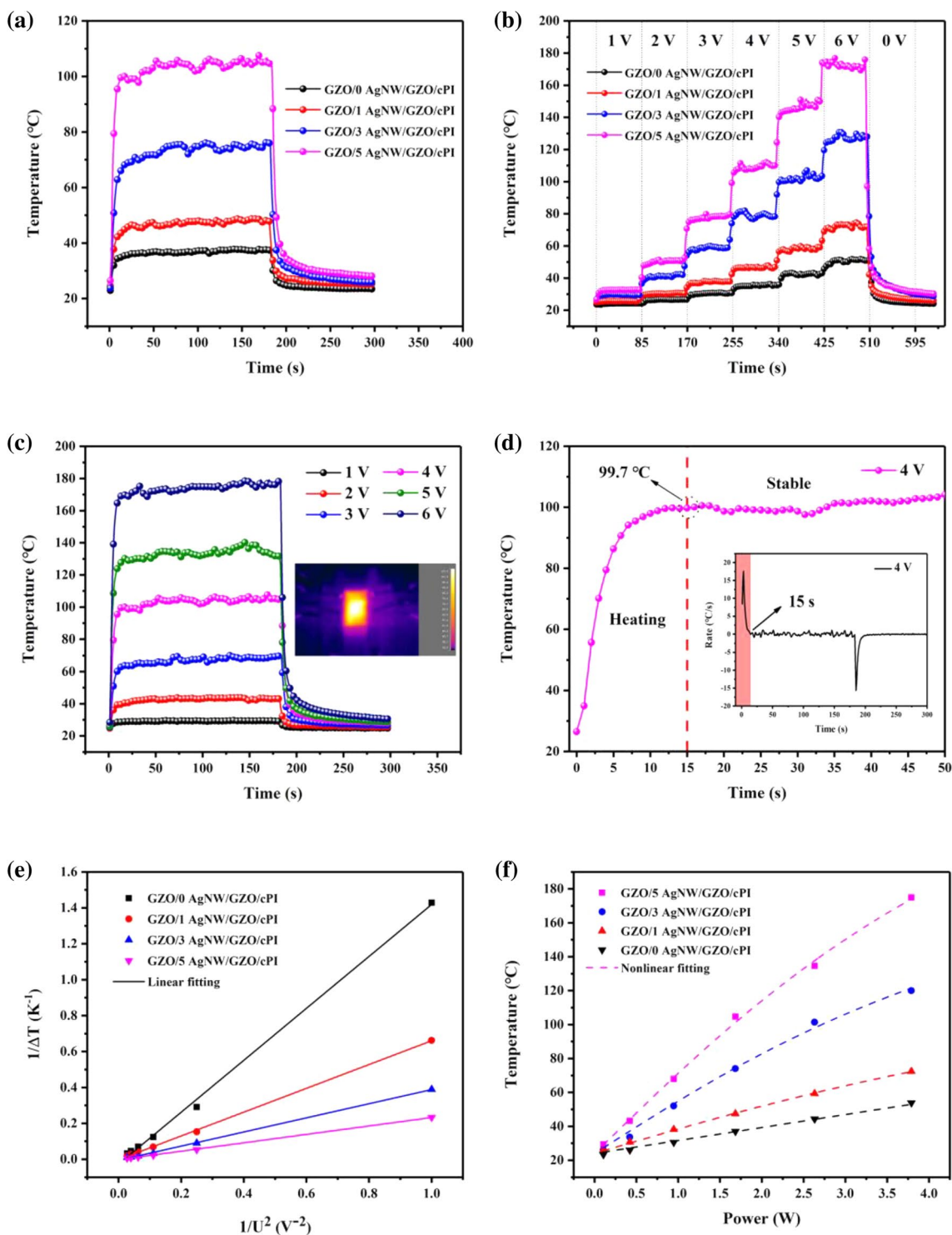


Fig. 5 a The temperature as a function of time for TFHs with different N at 4 V input voltage. **b** Temperature profiles of GZO/AgNW/GZO/cPI TFHs with different N carried out at incrementally increased biases. **c** Temperature change of GZO/5 AgNW/GZO/cPI hybrid TFHs at different applied voltages. Inset is the IR photograph

of TFH with R_0 of 9.5 Ω operated at 4 V. **d** Temperature change of GZO/5 AgNW/GZO/cPI hybrid TFH working at 4 V. Inset is the heating or cooling rate versus time. **e** The relationship between $1/\Delta T$ and $1/U^2$. **f** Variation of the steady-state temperature with input power

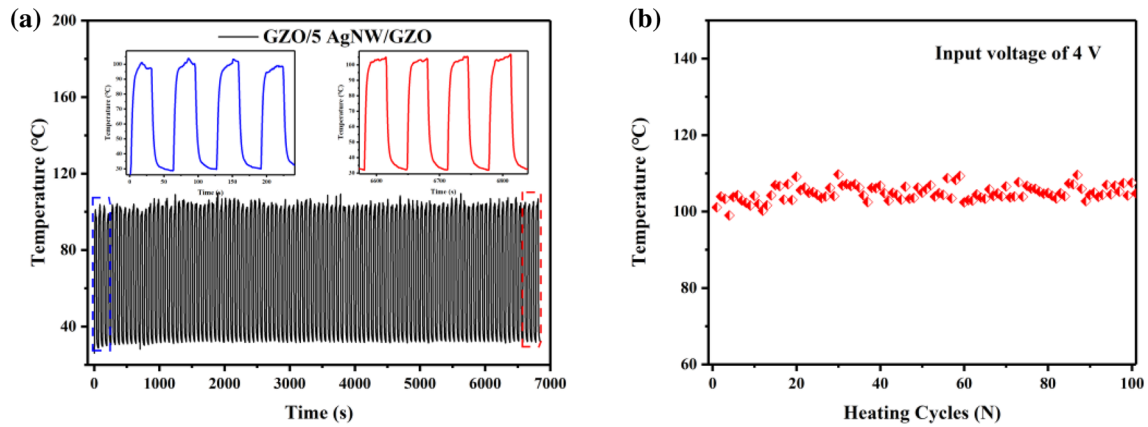


Fig. 6 **a** The cyclic thermal stability test and **b** the maximum temperature of GZO/5 AgNW/GZO/cPI TFH under 4 V

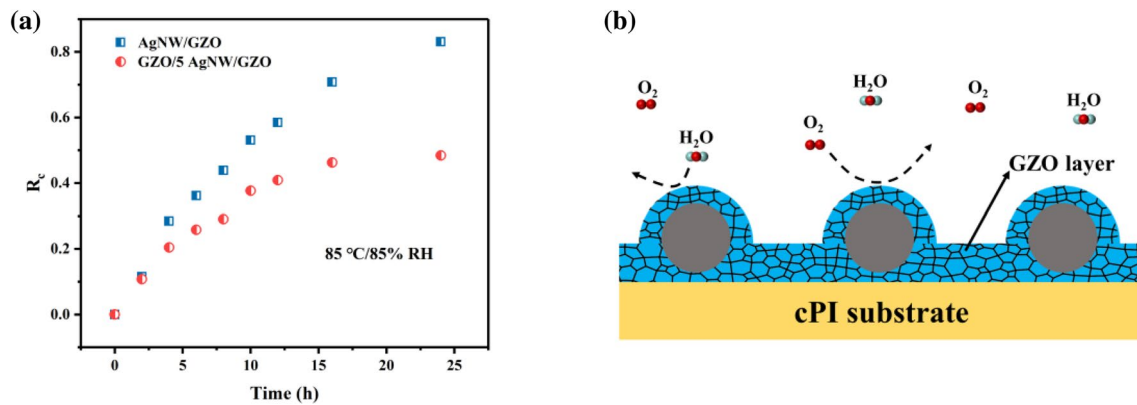


Fig. 7 **a** Temporal changes in the resistance of AgNW/GZO and GZO/AgNW/GZO films with R_0 of 13.0 Ω and 9.3 Ω , respectively, at 85 °C and 85% RH. **b** Schematic illustration of the protective function of GZO layer

4 Conclusions

In summary, flexible transparent conductive heaters based on GZO/AgNW/GZO sandwich structure have been prepared on cPI substrates. The conductivity and transmittance can be controlled by the content of AgNWs. Under the synergy of GZO and AgNWs, the flexible TFH can reach a high saturation temperature of 176.0 °C at an input voltage of 6 V and good thermal stability. GZO layer plays two roles in flexible TFH. Firstly, the GZO layer acts as a heat insulating layer. The heat exchange between AgNWs and surroundings is reduced and the thermal response time of TFH is accelerated. Secondly, the GZO layer acts as a protective layer to ensure the good stability of GZO/AgNW/GZO/cPI TFHs in harsh environments. These results indicate the great potential applications of GZO/AgNW/GZO/cPI TFHs in flexible electronic devices.

Acknowledgements This work was financial supported by the Program for the Ningbo Municipal Science and Technology Innovative Research Team (2016B10005), Zhejiang Provincial Natural Science Foundation of China (LY19A020002), and National Natural Science Foundation of China (61774160).

References

1. W. Lan, Y. Chen, Z. Yang, W. Han, J. Zhou, Y. Zhang, J. Wang, G. Tang, Y. Wei, W. Dou, Q. Su, E. Xie, ACS Appl. Mater. Interfaces **9**, 6644–6651 (2017)
2. H. Kim, M. Seo, J.W. Kim, D.K. Kwon, S.E. Choi, J.W. Kim, J.M. Myoung, Adv. Funct. Mater. **29**, 1901061 (2019)
3. S. Choi, J. Park, W. Hyun, J. Kim, J. Kim, Y.B. Lee, C. Song, H.J. Hwang, J.H. Kim, T. Hyeon, D.-H. Kim, ACS Nano **9**, 6626–6633 (2015)
4. J.J. Bae, S.C. Lim, G.H. Han, Y.W. Jo, D.L. Doung, E.S. Kim, S.J. Chae, T.Q. Huy, N. Van Luan, Y.H. Lee, Adv. Funct. Mater. **22**, 4819–4826 (2012)

5. X. He, A. Liu, X. Hu, M. Song, F. Duan, Q. Lan, J. Xiao, J. Liu, M. Zhang, Y. Chen, Q. Zeng, *Nanotechnology* **27**, 475709 (2016)
6. C. Celle, C. Mayousse, E. Moreau, H. Basti, A. Carella, J.-P. Simonato, *Nano Res.* **5**, 427–433 (2012)
7. R. Gupta, G.U. Kulkarni, *A.C.S. Appl. Mater. Interfaces* **5**, 730–736 (2013)
8. J. Jin, J. Lee, S. Jeong, S. Yang, J.-H. Ko, H.-G. Im, S.-W. Baek, J.-Y. Lee, B.-S. Bae, *Energy Environ. Sci.* **6**, 1811–1817 (2013)
9. A.Y. Kim, M.K. Kim, C. Hudaya, J.H. Park, D. Byun, J.C. Lim, J.K. Lee, *Nanoscale* **8**, 3307–3313 (2016)
10. S. Wang, X. Zhang, W. Zhao, *J. Nanomater.* **2013**, 1–6 (2013)
11. Y. Guo, C. Dun, J. Xu, J. Mu, P. Li, L. Gu, C. Hou, C.A. Hewitt, Q. Zhang, Y. Li, D.L. Carroll, H. Wang, *Small* **13**, 1702645 (2017)
12. W. Ning, Z. Wang, P. Liu, D. Zhou, S. Yang, J. Wang, Q. Li, S. Fan, K. Jiang, *Carbon* **139**, 1136–1143 (2018)
13. Y. Kim, H.R. Lee, T. Saito, Y. Nishi, *Appl. Phys. Lett.* **110**, 153301 (2017)
14. P. Zhang, I. Wyman, J.W. Hu, S.D. Lin, Z.W. Zhong, Y.Y. Tu, Z.Z. Huang, Y.L. Wei, *Mater Sci Eng B* **223**, 1–23 (2017)
15. J.S. Woo, J.T. Han, S. Jung, J.I. Jang, H.Y. Kim, H.J. Jeong, S.Y. Jeong, K.J. Baeg, G.W. Lee, *Sci. Rep.* **4**, 4804 (2014)
16. T. Kim, Y.W. Kim, H.S. Lee, H. Kim, W.S. Yang, K.S. Suh, *Adv. Funct. Mater.* **23**, 1250–1255 (2013)
17. X. Shi, W. Xu, W. Shen, G. Wang, R. Wang, X. Li, W. Song, *J. Mater. Sci.* **30**, 2089–2095 (2018)
18. H.-G. Cheong, D.-W. Song, J.-W. Park, *Microelectron. Eng.* **146**, 11–18 (2015)
19. Q.S. Xu, W.F. Shen, Q.J. Huang, Y. Yang, R.Q. Tan, K. Zhu, N. Dai, W.J. Song, *J. Mater. Chem. C* **2**, 3750–3755 (2014)
20. S.J. Choi, S.J. Kim, J.S. Jang, J.H. Lee, I.D. Kim, *Small* **12**, 5826–5835 (2016)
21. H.-G. Cheong, J.-H. Kim, J.-H. Song, U. Jeong, J.-W. Park, *Thin Solid Films* **589**, 633–641 (2015)
22. F. Xu, W. Xu, B.X. Mao, W.F. Shen, Y. Yu, R.Q. Tan, W.J. Song, *J. Colloid Interface Sci.* **512**, 208–218 (2018)
23. Y.-Y. Choi, K.-H. Choi, H. Lee, H. Lee, J.-W. Kang, H.-K. Kim, *Sol. Energy Mater. Sol. Cells* **95**, 1615–1623 (2011)
24. G. Haacke, *J. Appl. Phys.* **47**, 4086–4089 (1976)
25. Q.J. Huang, W.F. Shen, X.Z. Fang, G.F. Chen, Y. Yang, J.H. Huang, R.Q. Tan, W.J. Song, *A.C.S. Appl. Mater. Interfaces* **7**, 4299–4305 (2015)
26. S. Ji, W. He, K. Wang, Y. Ran, C. Ye, *Small* **10**, 4951–4960 (2014)
27. G.L. Wang, W. Xu, F. Xu, W.F. Shen, W.J. Song, *Mater. Res. Express* **4**, 116405 (2017)

Publisher's Note Springer Nature remains neutral with regard to jurisdictional claims in published maps and institutional affiliations.